Available online at www.sciencedirect.com
ScienceDirect
Comput. Methods Appl. Mech. Engrg. 196 (2006) 620–633
Computer methods in applied mechanics and engineering
www.elsevier.com/locate/cma

Finite element formulation for modeling particle debonding in reinforced elastomers subjected to finite deformations ☆

Karel Matouš *, Philippe H. Geubelle

Center for Simulation of Advanced Rockets, Department of Aerospace Engineering, University of Illinois at Urbana-Champaign, Urbana, IL 61801, USA

Received 20 July 2005; accepted 9 June 2006

Abstract

Interfacial damage nucleation and evolution in reinforced elastomers is modeled using a three-dimensional updated Lagrangian finite element formulation based on the perturbed Petrov–Galerkin method for the treatment of nearly incompressible behavior. The progressive failure of the particle–matrix interface is modeled by a cohesive law accounting for mode mixity. The meso-scale is characterized by a unit cell, which contains particles dispersed in a homogenized blend. A new, fully implicit and efficient finite element formulation, including consistent linearization, is presented. The proposed finite element model is capable of predicting the non-homogeneous meso-fields and damage nucleation and propagation along the particle–matrix interface. Simple deformations involving an idealized solid rocket propellant are considered to demonstrate the algorithm.

Keywords: Decohesion; Cohesive and volumetric elements; Stabilized method; Finite deformations; Particulate composites

1. Introduction

With examples ranging from automobile tires to solid propellants, particle-reinforced elastomers play an important role in a wide variety of engineering applications and the modeling of their constitutive response continues to be a long-standing research topic. The complexity of the modeling is associated with the combination of a large set of sometimes competing physical processes taking place at various length scales: large deformations of the quasi-incompressible elastomeric matrix, large stiffness mismatch between the matrix and the reinforcing particles, non-linear viscoelastic response of the elastomer, Mullins hysteretic effect under cyclic loading, particle debonding, void growth, matrix tearing, inter-particle interaction, etc.

The number and complexity of these phenomena have led most of the modeling efforts reported in the literature to rely on homogenized continuum models to capture some of these key features of the mechanical response. For example, Bergstrom and Boyce [2] have proposed a dual-network model to predict the non-linear viscoelastic response of carbon-black reinforced rubbers, with emphasis on capturing the large deformation and Mullins effects. Drozdov and Dorfmann [8] also used the network theory of rubber elasticity to capture the non-linear equilibrium response of filled and unfilled elastomers. Most theories, however, are based on phenomenological continuum models of various features of the constitutive response of filled elastomers. Examples include Dorfmann and Ogden's analysis of the Mullins effect [7], Kaliske and Rothert's work on the internal friction [13] and Miehe and Keck's stress decomposition model of damage evolution [25].

Another complexity is associated with the numerical treatment of these materials. As mentioned earlier, the matrix material is nearly incompressible and a special numerical formulation has to be employed. A mixed finite element method that interpolates the pressure and displace-

☆ US Department of Energy, B341494.
* Corresponding author. Tel.: +1 217 333 8448; fax: +1 217 333 8497.
E-mail addresses: matous@uiuc.edu (K. Matouš), geubelle@uiuc.edu (P.H. Geubelle).
URL: http://www.csar.uiuc.edu/~matous/ (K. Matouš).

0045-7825/$ - see front matter © 2006 Elsevier B.V. All rights reserved.
doi:10.1016/j.cma.2006.06.008

ment fields separately is required. For Galerkin methods, the choice of interpolation functions must satisfy the Babuška–Brezzi condition (see, e.g., [4]) in order to achieve uniqueness, convergence and robustness. Without balancing the interpolations properly, significant oscillations in the solution typically result. Considerable effort has been devoted in recent years to develop novel numerical techniques that give stable solution [23,37,5]. Especially, stabilized theories, where Babuška–Brezzi stability condition is circumvented, have been recently explored [16,17,27].

The primary focus of this research is to develop a computational model of damage evolution under high strain levels in highly filled elastomers such as solid propellants and other energetic materials, which are composed of particles of varying sizes (typically a bimodal distribution) needed to achieve a high energetic content. Various "homogenized" models have been proposed to simulate the damage evolution: see, for example, the analysis presented by Farris [11], Schapery [33], Ha and Schapery [14], Simo [36], Ravichandran and Liu [30]. Other approaches rely on micromechanics [22,18,38].

In these highly filled elastomers, experimental observations have shown that the failure process is primarily driven by the debonding of the larger particles, with the smaller particles playing the role of stiffener for the matrix [1,29]. Based on these observations, Zhong and Knauss [44,45] have used a cohesive finite element approach to simulate the progressive particle debonding process in simple 2D representative volume elements (RVE) composed of a few large rigid particles embedded in a non-linear elastic matrix. The emphasis of their work was to capture the effect of the inter-particle interaction and the influence of the interface cohesive properties on the evolution and stability of the dewetting process.

Building on Zhong and Knauss' work, we present a numerical study where the key emphases are: (1) the development and implementation of a 3D model under large deformations; (2) the accurate and efficient treatment of the near-incompressibility of the matrix through a stabilized finite element formulation; (3) the consistent linearization of the set of non-linear equilibrium equations leading to a very efficient algorithm.

In this paper, the interfacial damage is modeled by cohesive elements [28,31,12,43] and the stabilized Petrov–Galerkin formulation is used to describe the large incompressible deformations of a matrix [16,17]. The formulation and implementation of the mathematical theory of homogenization in finite strains is presented in paper by Matouš and Guebelle [24]. The presented work can also serve as a computational component in the embedded multiscale scheme proposed by Oden [26] for example.

The paper is organized as follows: In Section 2, we summarize the basic kinematic, equilibrium and constitutive relations that describe the problem, including the cohesive model characterized by an exponential traction–separation law that accounts for mode mixity. A stabilized variational framework based on an updated Lagrangian formulation is presented in Section 3, together with the finite element formulation and its consistent linearization. Section 4 describes constitutive laws characterizing the mechanical behavior of individual constituents. A few comments about the non-linear solver and an adaptive time stepping procedure are presented in Section 5, together with a few illustrative example involving the uniaxial loading of simple unit cells composed of one and four reinforcing particles.

The symbolic notation adopted herein uses upper case boldface italic and lower case boldface Greek letters, e.g., $\boldsymbol{P}$ and $\boldsymbol{\sigma}$ for second-order tensors. The trace of the second-order tensor is denoted as $\mathrm{tr}(\boldsymbol{A})$, and the tensor operations between two second-order tensors $\boldsymbol{S}$ and $\boldsymbol{E}$ are indicated as $\boldsymbol{SE}$ for a tensor contraction (a second-order tensor) or $\boldsymbol{S}:\boldsymbol{E}$ for the scalar product (a double contraction).

2. Finite strain irreversible cohesive law

Consider a hyperelastic body in an initial configuration $B_0 \subset \mathbb{R}^3$, which undergoes the motion $\boldsymbol{\phi}(\boldsymbol{X}, t)$ and let $\boldsymbol{F}(\boldsymbol{X},t) = \nabla\boldsymbol{\phi}(\boldsymbol{X},t)$ be the deformation gradient at the current time $t \in \mathbb{R}^+$ with the Jacobian given by $J = \det(\boldsymbol{F})$. Here $\boldsymbol{X} \in \mathbb{R}^3$ designates the position of a particle in the reference configuration $B_0 \subset \mathbb{R}^3$ in the Cartesian coordinate system. Suppose now that the body is divided by a cohesive surface S_0 with a unit normal $\boldsymbol{N}_0$ (Fig. 1). For the sake of simplicity, we assume that the cohesive surface partitions the body into two subbodies $B_0^{\pm}$, occupying the plus and minus sides of the cohesive surface, $S_0^{\pm}$, respectively.

Next, let $\boldsymbol{x} = \boldsymbol{\phi}(\boldsymbol{X},t)$ be the spatial coordinates of a particle and $\boldsymbol{x}_{n+1} = \boldsymbol{X} + \boldsymbol{u}_{n+1}$, where $\boldsymbol{u}_{n+1} = \boldsymbol{u}_n + \boldsymbol{u}$ denotes the incremental displacement field. Here and henceforth, right subscripts n and $n+1$ indicate times t_n and t_{n+1}, respectively. Using an *updated Lagrangian* formulation and adopting the multiplicative decomposition of the deformation gradient, we arrive at

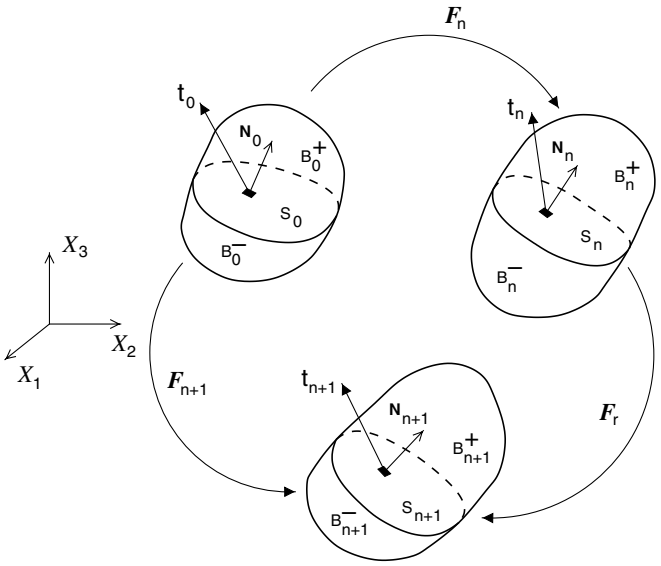

Fig. 1. Kinematic decomposition of deformation gradients.

$$\begin{aligned} \boldsymbol{F}_{n+1} &= \boldsymbol{F}_r \boldsymbol{F}_n, \\ \boldsymbol{F}_r &= \mathbf{1} + \nabla \boldsymbol{u}, \\ J_r &= \det(\boldsymbol{F}_r), \\ J_n &= \det(\boldsymbol{F}_n), \end{aligned} \tag{1}$$

where $\boldsymbol{F}_r$ represents the relative deformation gradient, $\nabla = \nabla_{x_n}$ is a gradient with respect to $\boldsymbol{x}_n$ and $\mathbf{1}$ denotes the second-order identity tensor.

Described in quantities of the updated configuration, the governing equations including the cohesive zone, yield

$$\begin{aligned} &\nabla \cdot \boldsymbol{P}_r + \boldsymbol{f}_n = \mathbf{0} && \text{in } B_n^{\pm}, \\ &\boldsymbol{P}_r \cdot \boldsymbol{N}_n = \bar{\boldsymbol{t}}_n && \text{on } \boldsymbol{\phi}(\partial B_{\boldsymbol{P}}), \\ &\boldsymbol{u} = \bar{\boldsymbol{u}} && \text{on } \boldsymbol{\phi}(\partial B_{\boldsymbol{u}}), \\ &\lfloor \boldsymbol{P}_r \cdot \boldsymbol{N}_n \rceil \equiv \lfloor \boldsymbol{t}_n \rceil = \mathbf{0} && \text{on } S_n^{\pm}, \end{aligned} \tag{2}$$

where $\boldsymbol{t}_n$ represents the cohesive tractions across S_n, $\boldsymbol{P}_r = J_r \boldsymbol{\sigma} \boldsymbol{F}_r^{-T}$ is the relative first Piola–Kirchhoff (P–K) stress, $\boldsymbol{\sigma}$ denoting the Cauchy stress on the deformed configuration $B_{n+1}^{\pm}$, $\boldsymbol{f}_n(\boldsymbol{x}_n)$ denotes the body forces and $\bar{\boldsymbol{t}}_n(\boldsymbol{x}_n)$ represents the prescribed tractions on the boundary $\boldsymbol{\phi}(\partial B_{\boldsymbol{P}})$. We also consider Dirichlet boundary conditions $\bar{\boldsymbol{u}}$ on $\boldsymbol{\phi}(\partial B_{\boldsymbol{u}})$. The symbol $\lfloor \bullet \rceil = (\bullet^{+} - \bullet^{-})$ denotes the jump of a quantity $\bullet$ across the cohesive surface.

Following standard variational methods, the principle of virtual work reads

$$\int_{B_n^{\pm}} \boldsymbol{P}_r : \nabla \delta \boldsymbol{u} \, \mathrm{d}V_n + \int_{S_n} \widetilde{J}_n \boldsymbol{t}_0 \cdot \lfloor \delta \boldsymbol{u} \rceil \, \mathrm{d}S_n - \int_{B_n^{\pm}} \boldsymbol{f}_n \cdot \delta \boldsymbol{u} \, \mathrm{d}V_n - \int_{\partial B_n^{\pm}} \bar{\boldsymbol{t}}_n \cdot \delta \boldsymbol{u} \, \mathrm{d}A_n = 0 \tag{3}$$

for all admissible variations $\delta \boldsymbol{u}$ satisfying

$$\delta \boldsymbol{u} \in \mathfrak{U} \subset [H^1]^{\mathfrak{N}}, \quad \delta \boldsymbol{u} = \mathbf{0} \quad \text{on } \boldsymbol{\phi}(\partial B_{\boldsymbol{u}}), \tag{4}$$

where $\mathfrak{N}$ being the space dimension and H^1 represents the Sobolev space.

The presence of a cohesive surface results in an additional term (second term in (3)) in the principle of virtual work, which can be deduced from the unbounded part of the gradient of the weighting function [41]; $\boldsymbol{t}_0$ represents the cohesive tractions across S_0 and $\widetilde{J}_n = \sqrt{\boldsymbol{N}_n \cdot (\boldsymbol{F}_n \boldsymbol{F}_n^T \boldsymbol{N}_n)}/J_n$ is the Jacobian of the transformation between the undeformed and the updated configurations. Moreover, it follows that tractions $\boldsymbol{t}_0$ do work on the displacement jumps or "opening displacements" defined over the cohesive surface as

$$\boldsymbol{\chi} \equiv \lfloor \boldsymbol{\phi}(\boldsymbol{X}, t) \rceil = \boldsymbol{\chi}_n + \lfloor \boldsymbol{u} \rceil. \tag{5}$$

Please note that $\boldsymbol{\chi}$ vanishes identically when the body undergoes a rigid transformation, as required of a proper deformation measure. The cohesive element is shown schematically in Fig. 2 together with the effective traction–separation law, which is described in what follows. Note that the discontinuity is always contained between volumetric elements as opposed to the Generalized finite element method [41]. Hence, the test functions lie in the space of bounded variations since they are discontinuous across the interface.

By recourse to Coleman and Noll's method [19,20] it is possible to show that the local tractions $\boldsymbol{t}_0$ take the form

$$\boldsymbol{t}_0 = \frac{\partial \psi}{\partial \boldsymbol{\chi}}. \tag{6}$$

It is worth noting in this regard that the cohesive free energy ψ is subject to the restrictions imposed by material frame indifference. Following the approach proposed by Ortiz and Pandolfi [28], the unique deformed cohesive surface S is defined in terms of the mean deformation mapping

$$\begin{aligned} \bar{\boldsymbol{\phi}}(\boldsymbol{X}, t) &= \frac{1}{2}[\boldsymbol{\phi}^{+}(\boldsymbol{X}, t) + \boldsymbol{\phi}^{-}(\boldsymbol{X}, t)], \\ \boldsymbol{\phi}^{\pm}(\boldsymbol{X}, t) &= \bar{\boldsymbol{\phi}}(\boldsymbol{X}, t) \pm \frac{1}{2}\boldsymbol{\chi}, \end{aligned} \tag{7}$$

and the traction separation law is given by

$$\boldsymbol{t}_0 = \frac{\tilde{t}}{\tilde{\chi}} \hat{\boldsymbol{t}}, \quad \hat{\boldsymbol{t}} = [\beta^2 \boldsymbol{\chi} + (1 - \beta^2)(\boldsymbol{\chi} \cdot \boldsymbol{N})\boldsymbol{N}], \tag{8}$$

where β assigns different weights to the sliding and normal opening displacements and $\boldsymbol{N}$ denotes the unit normal of the cohesive surface S.

The present work adopts the simple and computationally convenient cohesive law [28,31,43] (Fig. 2)

$$\psi = e \sigma_c \chi_c \left[1 - \left(1 + \frac{\tilde{\chi}}{\chi_c} \right) \mathrm{e}^{-\tilde{\chi}/\chi_c} \right], \quad \tilde{t} = \frac{\partial \psi}{\partial \tilde{\chi}} = e \sigma_c \frac{\tilde{\chi}}{\chi_c} \mathrm{e}^{-\tilde{\chi}/\chi_c}, \tag{9}$$

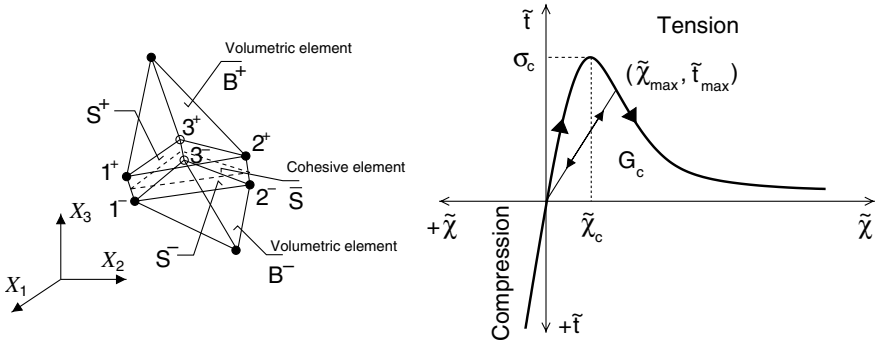

Fig. 2. Geometry of cohesive element and irreversible cohesive law.

where $e = \exp(1)$, χ_c denotes the characteristic opening displacement and σ_c is the maximum effective cohesive traction. The effective opening displacement $\tilde{\chi}$ is defined by

$$\tilde{\chi} = \sqrt{\beta^2 \tilde{\chi}_s^2 + \tilde{\chi}_n^2}, \tag{10}$$

while the normal and tangential displacement jump components are

$$\tilde{\chi}_n = \boldsymbol{\chi} \cdot \boldsymbol{N}, \quad \tilde{\chi}_s = |\boldsymbol{\chi}_s|, \quad \boldsymbol{\chi}_s = (\mathbf{1} - \boldsymbol{N} \otimes \boldsymbol{N})\boldsymbol{\chi}, \tag{11}$$

where $\otimes$ denotes dyadic product. As in Ortiz and Pandolfi [28], we shall assume loading if $\tilde{\chi} = \tilde{\chi}_{\max}$ and $\dot{\tilde{\chi}} \geqslant 0$. The evolution of the internal state variable, $\tilde{\chi}_{\max}$, is given by

$$\dot{\tilde{\chi}}_{\max} = \begin{cases} \dot{\tilde{\chi}} & \text{if } \tilde{\chi} = \tilde{\chi}_{\max} \text{ and } \dot{\tilde{\chi}} \geqslant 0 \\ 0 & \text{otherwise.} \end{cases} \tag{12}$$

We also assume unloading to be directed toward the origin (Fig. 2), giving

$$\tilde{t} = \frac{\tilde{t}_{\max}}{\tilde{\chi}_{\max}} \tilde{\chi} \quad \text{if } \tilde{\chi} < \tilde{\chi}_{\max} \text{ or } \dot{\tilde{\chi}} < 0. \tag{13}$$

For the cohesive model described by (9), the cohesive fracture energy per unit area of the cohesive surface is given by

$$G_c = \int_0^\infty \tilde{t}\, \mathrm{d}\tilde{\chi} = e\sigma_c \chi_c. \tag{14}$$

It bears emphasis that, upon closure, the cohesive surfaces are subjected to a (possibly frictional) contact constraint. Instead of a more complex numerical treatment of the contact between the crack faces, such as in Simo et al. [34], we enforce the contact constraint with the aid of a non-sliding (stick) exponentially increasing compressive constraint on the effective cohesive traction (Fig. 2):

$$\tilde{t} = \tilde{\chi}\sigma_c \frac{\tilde{\chi} + \chi_c}{\chi_c^2} \mathrm{e}^{\frac{\tilde{\chi}+\chi_c}{\chi_c}}, \quad \forall \tilde{\chi} > 0, \quad \text{if } \tilde{\chi}_n < 0. \tag{15}$$

Please note that the effective opening displacement and effective tractions are always positive, that contact is detected for negative normal opening displacement, $\tilde{\chi}_n < 0$, and that the first derivatives of (9_b) and (15) evaluated at $\tilde{\chi} = 0$ are identical.

3. Stabilized finite element formulation

We now outline the variational formulation and numerical treatment by the finite element method of the elliptic boundary value problem described above, with special emphasis on the derivation of a consistent linearization of the non-linear problem and on the accurate numerical treatment of the near-incompressible response of a matrix.

On the latter issue, the present finite element procedure is based on a stabilized Petrov–Galerkin formulation to treat volume constraints arising from the nearly incompressible hyperelastic material behavior. Employing the additive decomposition of the free energy density into distortional and volumetric components

$$W(\boldsymbol{C}) = \widehat{W}(\boldsymbol{C}) + U(J), \tag{16}$$

the second Piola–Kirchhoff tensor in the reference configuration is obtained in the standard manner:

$$\begin{aligned} \boldsymbol{S}_0 &= 2\frac{\partial \widehat{W}}{\partial \boldsymbol{C}} + \gamma J \boldsymbol{C}^{-1}, \\ \gamma &= \frac{\partial U}{\partial J}, \end{aligned} \tag{17}$$

where $\boldsymbol{C} = \boldsymbol{F}^{\mathrm{T}}\boldsymbol{F}$ denotes the Cauchy–Green deformation tensor. Note that the scalar multiplier γ is equal to the hydrostatic stress "pressure", $\gamma \equiv p = 1/3\ \mathrm{tr}(\boldsymbol{\sigma})$, only if the energy density is a homogeneous function of zeroth order [3]. We can therefore express the energy function W in terms of the distortional component of the right Cauchy–Green tensor $\widehat{\boldsymbol{C}} = (\det \boldsymbol{C})^{-1/3}\boldsymbol{C}$ to give a formally modified energy functional $\widehat{W}(\boldsymbol{C}) = W(\widehat{\boldsymbol{C}})$. Details of this substitution are derived in [3] and the same approach was used by Klaas et al. [17]. The relative first P–K stress $\boldsymbol{P}_r$ and the second P–K stress $\boldsymbol{S}_n$ on $B_n^{\pm}$ can be written as

$$\begin{aligned} \boldsymbol{P}_r &= \boldsymbol{F}_r \boldsymbol{S}_n, \\ \boldsymbol{S}_n &= \phi_*[\boldsymbol{S}_0] = \frac{1}{J_n}\boldsymbol{F}_n \widetilde{\boldsymbol{S}} \boldsymbol{F}_n^T + pJ_r \boldsymbol{F}_r^{-1}\boldsymbol{F}_r^{-T}, \end{aligned} \tag{18}$$

where $\phi_*[\boldsymbol{S}_0]$ refers to the push-forward operation and $\widetilde{\boldsymbol{S}}$ denotes the deviatoric part of $\boldsymbol{S}_0$. In this work, we use the simple volumetric function $U(J)$:

$$\begin{aligned} U(J) &= \frac{1}{2}\kappa(J-1)^2, \\ p &= \kappa(J-1), \end{aligned} \tag{19}$$

where κ is the bulk modulus and the relative pressure over an increment, $\boldsymbol{u}$, is given by

$$\tilde{p} = p_{n+1} - p_n = \kappa[J_n(J_r - 1)]. \tag{20}$$

The distortional component of the free density function is introduced later in Section 4.

As described by Klaas et al. [17], mesh-dependent terms that are functions of the Euler–Lagrange equations from finer scale are added to the variational statement (3) and the pressure p is interpolated as an independent variable. In particular, the push-forward of the gradient of pressure weighting function, $\boldsymbol{F}_r^{-T}\nabla\delta\tilde{p}$, is used to perturb the Galerkin weighting space. Thus, the strong form of equilibrium equations (2) is integrated with the weighting function

$$\delta\boldsymbol{v} = \delta\boldsymbol{u} + \Theta \boldsymbol{F}_r^{-T}\nabla\delta\tilde{p}, \tag{21}$$

where the perturbation is applied element-wise and Θ is chosen following Hughes et al. [16] as

$$\Theta = \frac{\omega h_e^2}{2\mu}. \tag{22}$$

Here, h_e denotes the characteristic element length, μ represents the shear modulus of the material and ω is a non-dimensional, non-negative stability parameter.

Using the standard variational procedure, inserting (18) into (2), taking (21) into account and enforcing (20) in a

weak sense, we obtain the following stabilized mixed formulation:

$$\begin{aligned}
\mathscr{R}_{\boldsymbol{u}} &\equiv \int_{B_n^{\pm}} \frac{1}{J_n}(\boldsymbol{F}_n\widetilde{\boldsymbol{S}}\boldsymbol{F}_n^T) : (\boldsymbol{F}_r^T\nabla\delta\boldsymbol{u})\,\mathrm{d}V_n \\
&\quad + \int_{B_n^{\pm}} J_r p\boldsymbol{F}_r^{-T} : (\nabla\delta\boldsymbol{u})\,\mathrm{d}V_n + \int_{S_n} \widetilde{J}_n\boldsymbol{t}_0\cdot\lfloor\delta\boldsymbol{u}\rceil\,\mathrm{d}S_n \\
&\quad - \int_{B_n^{\pm}} \boldsymbol{f}_n\cdot\delta\boldsymbol{u}\,\mathrm{d}V_n - \int_{\partial B_n^{\pm}} \bar{\boldsymbol{t}}_n\cdot\delta\boldsymbol{u}\,\mathrm{d}A_n = 0, \\
\mathscr{R}_p &\equiv \int_{B_n^{\pm}} \left[J_n(J_r-1) - \frac{\tilde{p}}{\kappa}\right]\delta\tilde{p}\,\mathrm{d}V_n \\
&\quad - \sum_{el}^{ne} \Theta \int_{B_n^e} J_r(\boldsymbol{F}_r^{-1}\boldsymbol{F}_r^{-T}) : (\nabla\tilde{p}\otimes\nabla\delta\tilde{p})\,\mathrm{d}V_n^e \\
&\quad + \sum_{el}^{ne} \Theta \int_{B_n^e} \left(\underbrace{\nabla\cdot\left[\frac{1}{J_n}\boldsymbol{F}_{n+1}\widetilde{\boldsymbol{S}}\boldsymbol{F}_n^T\right]}_{=0 \text{ for } P_1/P_1 \text{ elements}}\right)\cdot(\boldsymbol{F}_r^{-T}\nabla\delta\tilde{p})\,\mathrm{d}V_n^e = 0,
\end{aligned} \tag{23}$$

where ne denotes the number of elements and $\delta\boldsymbol{u}, \delta\tilde{p}$, are arbitrary functions satisfying

$$\begin{aligned}
&\delta\boldsymbol{u} \in \mathfrak{U}, \quad \delta\boldsymbol{u} = \boldsymbol{0} \quad \text{on} \quad \boldsymbol{\phi}(\partial B_{\boldsymbol{u}}), \\
&\delta\tilde{p} \in L_2.
\end{aligned} \tag{24}$$

In particular, equal-order interpolations for the displacement and pressure (e.g., P_1/P_1) are supported by the present formulation. Due to the linear interpolation of the displacement field, the last term in (23_b) is zero. Please note that reduction from an updated formulation to total Lagrangian formulation can be obtained easily by substituting $\boldsymbol{F}_n = \boldsymbol{1}$, $J_n = 1$, $\boldsymbol{F}_r = \boldsymbol{F}$, $J_r = J$ and integrating over the initial domain $B_0^{\pm}$. For a more detailed description of mixed and stabilized formulations, see [5,23,17].

3.1. Consistent linearization

The finite element method together with an arc-length procedure is applied to solve the non-linear system of equations (23). The formulation of a consistent tangent stiffness tensor is therefore essential to maintain a quadratic rate of convergence [35]. A consistent linearization for the set of non-linear equations about a configuration $(\boldsymbol{u}, \tilde{p})$ yields

$$\begin{aligned}
D\mathscr{R}_{\boldsymbol{u}}[\Delta\boldsymbol{u}] + D\mathscr{R}_{\boldsymbol{u}}[\Delta\tilde{p}] &= -\mathscr{R}_{\boldsymbol{u}}, \\
D\mathscr{R}_p[\Delta\boldsymbol{u}] + D\mathscr{R}_p[\Delta\tilde{p}] &= -\mathscr{R}_p,
\end{aligned} \tag{25}$$

where

$$\begin{aligned}
&D\mathscr{R}_{\boldsymbol{u}}[\Delta\boldsymbol{u}] \\
&= \int_{B_n^{\pm}} \frac{1}{J_n}\Bigg\{\underbrace{[\boldsymbol{F}_{n+1}^T(\nabla\delta\boldsymbol{u})\boldsymbol{F}_n] : \mathscr{L} : [\nabla(\Delta\boldsymbol{u})]}_{\text{material contribution}} + \underbrace{[\boldsymbol{F}_n^T(\nabla\delta\boldsymbol{u})^T\nabla(\Delta\boldsymbol{u})\boldsymbol{F}_n] : \widetilde{\boldsymbol{S}}}_{\text{geometric contribution}} \\
&\quad + \underbrace{pJ_rJ_n[\mathrm{tr}(\boldsymbol{F}_r^{-1}\nabla(\Delta\boldsymbol{u}))\mathrm{tr}(\boldsymbol{F}_r^{-1}\nabla\delta\boldsymbol{u}) - \mathrm{tr}(\boldsymbol{F}_r^{-1}\nabla(\Delta\boldsymbol{u})\boldsymbol{F}_r^{-1}\nabla\delta\boldsymbol{u})]}_{\text{pressure geometric contribution}}\Bigg\}\mathrm{d}V_n \\
&\quad + \int_{S_n} \underbrace{\widetilde{J}_n D\boldsymbol{t}_0[\Delta\boldsymbol{u}^{\pm}]\cdot\lfloor\delta\boldsymbol{u}\rceil}_{\text{cohesive model contribution}}\,\mathrm{d}S_n,
\end{aligned}$$

$$\begin{aligned}
D\mathscr{R}_{\boldsymbol{u}}[\Delta\tilde{p}] &= \int_{B_n^{\pm}} J_r\mathrm{tr}(\boldsymbol{F}_r^{-1}\nabla\delta\boldsymbol{u})\Delta\tilde{p}\,\mathrm{d}V_n, \\
D\mathscr{R}_{\tilde{p}}[\Delta\boldsymbol{u}] &= \int_{B_n^{\pm}} J_rJ_n\mathrm{tr}(\boldsymbol{F}_r^{-1}\nabla(\Delta\boldsymbol{u}))\delta\tilde{p}\,\mathrm{d}V_n \\
&\quad - \sum_{el}^{ne}\Theta\int_{B_n^e} J_r[\mathrm{tr}(\boldsymbol{F}_r^{-1}\nabla(\Delta\boldsymbol{u}))\boldsymbol{F}_r^{-1}\boldsymbol{F}_r^{-T} \\
&\quad - \boldsymbol{F}_r^{-1}\nabla(\Delta\boldsymbol{u})\boldsymbol{F}_r^{-1}\boldsymbol{F}_r^{-T}\boldsymbol{F}_r^{-1}\boldsymbol{F}_r^{-T} \\
&\quad (\nabla(\Delta\boldsymbol{u}))^T\boldsymbol{F}_r^{-T}] : [\nabla\tilde{p}\otimes\nabla\delta\tilde{p}]\,\mathrm{d}V_n^e, \\
D\mathscr{R}_p[\Delta\tilde{p}] &= -\int_{B_n^{\pm}} \frac{1}{\kappa}\delta\tilde{p}\Delta\tilde{p}\,\mathrm{d}V_n \\
&\quad - \sum_{el}^{ne}\Theta\int_{B_n^e} J_r[\boldsymbol{F}_r^{-1}\boldsymbol{F}_r^{-T}] : [\nabla(\Delta\tilde{p})\otimes\nabla\delta\tilde{p}]\,\mathrm{d}V_n^e,
\end{aligned} \tag{26}$$

with the tangent hyperelastic pseudo-moduli given by

$$\mathscr{L} = 2\frac{\partial\widetilde{\boldsymbol{S}}}{\partial\boldsymbol{C}} \mathscr{A} = \mathscr{C}\mathscr{A}. \tag{27}$$

Here we use the notation $\mathscr{A}$ for the fourth-order tensor $1/2(\partial\boldsymbol{C}/\partial\boldsymbol{F}_r)$. The deviatoric part of the material stiffness tensor $\mathscr{C} = 2\partial\widetilde{\boldsymbol{S}}/\partial\boldsymbol{C}$ is derived for a particular free density function in Section 4. The notation $\mathscr{R}_{\boldsymbol{y}}^{k+1} \approx \mathscr{R}_{\boldsymbol{y}}^k + D\mathscr{R}_{\boldsymbol{y}}[\Delta\boldsymbol{y}] = \boldsymbol{0}$ is employed in this paper for the consistent linearization of a non-linear system $\mathscr{R}_{\boldsymbol{y}} = \boldsymbol{0}$, where a solution $\boldsymbol{y}^{k+1} = \boldsymbol{y}^k + \Delta\boldsymbol{y}$ at iteration $k+1$ is obtained using an arc-length method. The resulting tangent stiffness tensor is non-symmetric in the present analysis. Several finite element approximation schemes can be used within the proposed variational framework provided by (23). In this work, continuous displacement and pressure interpolations are assumed, i.e., we use the so-called P_1/P_1 elements. The system of linear equations (25) is solved using the sparse direct solver UMFPACK [6]. The last missing component is the consistent linearization of the cohesive model contribution, $D\boldsymbol{t}_0[\Delta\boldsymbol{u}^{\pm}]$, present in (26_a). This term is described next.

3.2. Consistent linearization of cohesive model contribution

Let us first recall that the cohesive surface contribution in the principle of the virtual work is

$$\int_{S_n} \widetilde{J}_n\boldsymbol{t}_0\cdot\lfloor\delta\boldsymbol{u}\rceil\,\mathrm{d}S_n \equiv \int_{S_n} \widetilde{J}_n\frac{\tilde{t}}{\tilde{\chi}}\hat{\boldsymbol{t}}\cdot\lfloor\delta\boldsymbol{u}\rceil\,\mathrm{d}S_n \tag{28}$$

with the displacement jump and its weighting function defined by

$$\begin{aligned}
&\boldsymbol{\chi} = \boldsymbol{\chi}_n + (\boldsymbol{u}^+ - \boldsymbol{u}^-), \\
&\lfloor\delta\boldsymbol{u}\rceil \equiv \delta\boldsymbol{u}^+ - \delta\boldsymbol{u}^-.
\end{aligned} \tag{29}$$

In addition, we recall that the cohesive tractions $\boldsymbol{t}_0$ are dependent on both the opening displacement $\boldsymbol{\chi}$ and the normal $\boldsymbol{N}$:

$$\boldsymbol{t}_0 = \boldsymbol{t}_0(\boldsymbol{\chi}, \boldsymbol{N}). \tag{30}$$

Following the framework outlined in Section 2, all geometrical operations such as the computation of the normal, $\boldsymbol{N}$, are carried out on the middle surface $\overline{S}$ with coordinates

$$\bar{\boldsymbol{x}}_{n+1} = \bar{\boldsymbol{x}}_n + \frac{1}{2}(\boldsymbol{u}^+ + \boldsymbol{u}^-). \tag{31}$$

The normal is expressed in terms of the tangent basis vectors $\boldsymbol{e}_1$ and $\boldsymbol{e}_2$ as

$$\boldsymbol{N} = \frac{\boldsymbol{e}_1 \times \boldsymbol{e}_2}{|\boldsymbol{e}_1 \times \boldsymbol{e}_2|}, \tag{32}$$

where $\boldsymbol{e}_1$ and $\boldsymbol{e}_2$ are obtained using the standard isoparamatric element procedure, i.e., $\boldsymbol{e}_1 = \partial\bar{\boldsymbol{x}}/\partial\boldsymbol{x}_1$, $\boldsymbol{e}_2 = \partial\bar{\boldsymbol{x}}/\partial\boldsymbol{x}_2$.

The linearized cohesive model contribution is then

$$D\boldsymbol{t}_0[\Delta\boldsymbol{u}^{\pm}] = \frac{\partial \boldsymbol{t}_0}{\partial \boldsymbol{\chi}} \frac{\partial \boldsymbol{\chi}}{\partial \boldsymbol{u}^{\pm}} \Delta\boldsymbol{u}^{\pm} + \frac{\partial \boldsymbol{t}_0}{\partial \boldsymbol{N}} \frac{\partial \boldsymbol{N}}{\partial \bar{\boldsymbol{x}}} \frac{\partial \bar{\boldsymbol{x}}}{\partial \boldsymbol{u}^{\pm}} \Delta\boldsymbol{u}^{\pm}, \tag{33}$$

where, based on (8)–(10) and (32)

$$\begin{aligned}
\frac{\partial \boldsymbol{t}_0}{\partial \boldsymbol{\chi}} &= \frac{\psi''\tilde{\chi} - \tilde{t}}{\tilde{\chi}^3} \hat{\boldsymbol{t}} \otimes \hat{\boldsymbol{t}} + \frac{\tilde{t}}{\tilde{\chi}} [\beta^2 \mathbf{1} + (1-\beta^2) \boldsymbol{N} \otimes \boldsymbol{N}], \\
\frac{\partial \boldsymbol{t}_0}{\partial \boldsymbol{N}} &= \frac{\psi''\tilde{\chi} - \tilde{t}}{\tilde{\chi}^3} [\beta^2 (\boldsymbol{\chi} \cdot \boldsymbol{N})^2 \boldsymbol{N} + (1-\beta^2)(\boldsymbol{\chi} \cdot \boldsymbol{N})\boldsymbol{\chi}] \otimes \hat{\boldsymbol{t}} \\
&\quad + \frac{\tilde{t}}{\tilde{\chi}} (1-\beta^2)[\boldsymbol{\chi} \otimes \boldsymbol{N} + (\boldsymbol{\chi} \cdot \boldsymbol{N})\mathbf{1}], \\
\frac{\partial \boldsymbol{N}}{\partial \bar{\boldsymbol{x}}} &= \frac{\mathbf{1} - (\boldsymbol{N} \otimes \boldsymbol{N})}{|\boldsymbol{e}_1 \times \boldsymbol{e}_2|} \frac{\partial (\boldsymbol{e}_1 \times \boldsymbol{e}_2)}{\partial \bar{\boldsymbol{x}}},
\end{aligned} \tag{34}$$

and

$$\psi'' \equiv \frac{\partial^2 \psi}{\partial \tilde{\chi}^2} = \frac{\partial \tilde{t}}{\partial \tilde{\chi}} = \frac{\sigma_c e^{\left(-\frac{\tilde{\chi}-\chi_c}{\chi_c}\right)} (\chi_c - \tilde{\chi})}{\chi_c^2}. \tag{35}$$

Please recall that $\mathbf{1}$ is the second-order identity tensor and $\otimes$ denotes the dyadic product. Finally, a simple calculation gives

$$\frac{\partial \boldsymbol{\chi}}{\partial \boldsymbol{u}^{\pm}} = \mathbf{1}^{+} - \mathbf{1}^{-} \quad \text{and} \quad \frac{\partial \bar{\boldsymbol{x}}}{\partial \boldsymbol{u}^{\pm}} = \frac{1}{2}(\mathbf{1}^{+} + \mathbf{1}^{-}). \tag{36}$$

4. Constitutive laws

Although the model developed in this work pertains to many reinforced elastomeric materials, we focus our attention in the examples presented hereafter on the damage evolution in an idealized solid propellant composed of Ammonium Perchlorate (AP) particles embedded in a rubbery binder. As mentioned earlier, to achieve high energy content, solid propellants are typically characterized by high particle volume fractions obtained through a bimodal distribution of particle sizes. The small particles have a mean diameter of about 20 μm, while that of the larger particles is in the 100–300 μm range.

As described in the introductory section, damage initiation in these materials is often associated with the debonding of the larger particles and the role of the smaller ones is primarily to stiffen the binder. In the examples presented below, we assume a 64% concentration of AP particles, with 34% of large particles. The remaining 30% of small particles is then combined with the 36% of binder to create a homogenized matrix (blend).

To capture the mechanical behavior of the compressible AP particles and the nearly incompressible matrix, two hyperelastic material models are introduced. These models differ by the expression of the deviatoric component of their free energy density function: the functional form of the volumetric contribution is the same for both AP particles and the blend and is given by the simple relation (19).

4.1. AP particles

The deviatoric behavior of particles is described by the following distortional component of the free density function

$$\widehat{W} = \mu \boldsymbol{E} : \boldsymbol{E}, \tag{37}$$

where $\boldsymbol{E} = 1/2(\boldsymbol{C} - \mathbf{1})$ is the Green-Lagrange strain tensor, μ denotes the shear modulus and the deviatoric part of the second P–K stress reads

$$\widetilde{\boldsymbol{S}} = 2\mu \boldsymbol{E} = \mu(\boldsymbol{C} - \mathbf{1}). \tag{38}$$

For this model, the Lagrangian tensor $\mathscr{C}$ entering (27) is given by

$$\mathscr{C} = 2\mu \boldsymbol{I}, \tag{39}$$

where $\boldsymbol{I}$ denotes the fourth-order identity tensor.

4.2. Homogenized blend

The homogenized matrix is modeled as a nearly incompressible Neo-Hookean material with the distortional component of the free density function given by

$$\widehat{W} = \frac{1}{2}\mu[\mathrm{tr}(\hat{\boldsymbol{C}}) - 3], \quad \hat{\boldsymbol{C}} = (\det \boldsymbol{C})^{-1/3} \boldsymbol{C}, \tag{40}$$

where μ denotes the shear modulus obtained from homogenization. The deviatoric part of the second P–K stress is then given by

$$\widetilde{\boldsymbol{S}} = \mu(\det \boldsymbol{C})^{-1/3} \left[\mathbf{1} - \frac{1}{3}\mathrm{tr}(\boldsymbol{C})\boldsymbol{C}^{-T}\right]. \tag{41}$$

The corresponding expression of the fourth-order Lagrangian tensor $\mathscr{C}$ is

$$\begin{aligned}
\mathscr{C} = 2\mu(\det \boldsymbol{C})^{-1/3} \Big[&\frac{1}{9}\mathrm{tr}(\boldsymbol{C})\boldsymbol{C}^{-1} \otimes \boldsymbol{C}^{-1} - \frac{1}{3}\mathbf{1} \otimes \boldsymbol{C}^{-1} \\
&- \frac{1}{3}\boldsymbol{C}^{-1} \otimes \mathbf{1} + \frac{1}{3}\mathrm{tr}(\boldsymbol{C})\mathscr{B}\Big],
\end{aligned} \tag{42}$$

where the fourth-order tensor $\mathscr{B}$ in indicial notation reads

$$\mathscr{B}_{IJMN} = C^{-1}_{NI} C^{-1}_{JM}. \tag{43}$$

The homogenized mechanical properties of a blend, (μ, κ), are obtained by a homogenization procedure. As pointed out by Dvorak et al. [9], various estimates of the composite stiffness $\overline{\boldsymbol{L}}$ of any statistically homogeneous representative volume element (RVE) consisting of $r = 1, 2, \ldots, N$ phases can be written as

$$\overline{\boldsymbol{L}} = \left[\sum_{r=1}^{N} c_r (\boldsymbol{L}^* + \boldsymbol{L}_r)^{-1}\right]^{-1} - \boldsymbol{L}^*, \tag{44}$$

where c_r and $\boldsymbol{L}_r$, respectively, denote the volume fraction and elastic stiffness of constituent r; $\boldsymbol{L}^* = \boldsymbol{L}_0\mathscr{S}^{-1}(\boldsymbol{I} - \mathscr{S})$ corresponds to Hill's constraint tensor, $\boldsymbol{L}_0$ represents the stiffness of a comparison medium, $\mathscr{S}$ is the Eshelby tensor [10] and $\boldsymbol{I}$ is the identity matrix. Moreover, Walpole [39,40] proved that (44) satisfies the Hashin–Shtrikman [15] first-order variational bounds on the actual overall elastic properties, where the bounds $\overline{\boldsymbol{L}}^+$ and $\overline{\boldsymbol{L}}^-$ on the actual stiffness $\overline{\boldsymbol{L}}$ are obtained by selecting the stiffness $\boldsymbol{L}_0$ of a comparison medium. In this work, we adopt the Mori-Tanaka homogenization scheme for the blend, in which the binder serves as the comparison medium, i.e., $\boldsymbol{L}_0 = \boldsymbol{L}_m$. This assumption provides a lower bound on the overall compliance of the composite medium.

5. Examples

To illustrate and verify the proposed numerical framework, we now analyze the damage evolution in two model particulate composite systems. In the first one, which is composed of a single embedded particle, we focus on the debonding process along the particle/blend interface, with emphasis on the effect of the cohesive properties on the damage process and the existence of bifurcation in the solution. In the second example, we consider a four-particle composite system and demonstrate the ability of the numerical scheme to capture the effects of non-uniform particle spacing and size.

It is important to note, however, that, in the examples presented in this section, the finite element analysis enforces strictly homogeneous boundary conditions on the heterogeneous medium. This simple choice of boundary conditions affects the extracted average constitutive properties, presented below in terms of load multiplier versus axial displacement curves. This so-called embedded scheme, which was also used by Zhong and Knauss [44,45] in their 2D analysis, does not therefore lead to truly multiscale constitutive results, but can be used as a computational engine for embedded multiscale models [26]. The derivation and implementation of a mathematically consistent homogenization scheme were presented by Matouš and Geubelle [24]. The primary focus of the examples presented hereafter is to demonstrate the ability of the numerical scheme to capture the key features of the dewetting process.

All constituents are assumed to be isotropic hyperelastic solids with the free energy density functions described in Section 4. The elastic moduli of the various components, including those of the homogenized blend, are listed in Table 1. All finite element meshes are composed of four-node tetrahedral elements and have been generated using the *T3D* generator developed by Rypl [32]. The stability parameter ω entering (22) was set to one. For finite elasticity, this value was shown to be satisfactory [17] and no pressure oscillations were observed.

As mentioned earlier, the arc-length method is used to solve the non-linear system of equations (25). The arc-length procedure proposed by Simo et al. [34] was adopted in this work. Although the present finite element method is fully implicit and the time step is therefore mainly limited by considerations of convergence and accuracy of the solution of the non-linear equations, we implemented a simple time stepping procedure based on subdivision of a user-defined loading history [23]. The automatic time stepping procedure is robust and quickly finds the optimal time and load sub-increments for a given load path and a maximum number of iterations.

Table 1
Mechanical properties of individual constituents

Constituent	E^* [MPa]	μ [MPa]	ν
AP particle	32.447×10^3	14.19×10^3	0.1433
Binder	2.400	0.8003	0.4995
Homogenized blend	7.393	2.4656	0.4991

Two types of interfaces are considered; a strong interface (referred as Interface 1) and a weak one (Interface 2), characterized by the cohesive parameters listed in Table 2.

5.1. One-particle composite system

The geometry and boundary conditions for the one-particle system are presented in Fig. 3. A cubic unit cell consisting of a single AP spherical particle is loaded proportionally in tension. The displacements at the top and bottom surfaces of the unit cell are fixed in the x_1– x_2 plane. The bottom surface was fixed in x_3 direction also, and the top surface was proportionally loaded, $T = \lambda T_0$, by the load multiplier λ, through a rigid plate to ensure the uniform displacement in the x_3 direction. The reference axial force $T_0 = 8100\ \mu\text{N}$ was uniformly distributed over the top rigid surface.

Convergence studies involving cohesive finite element models have indicated that, for the case of interfacial failure, at least three cohesive elements have to be present in the active cohesive zone in front of the advancing crack front to achieve mesh independence. The expression of the cohesive zone size for the debonding of a curve bimaterial interface is not available. We have instead opted, for a rough estimate, the classical expression of the cohesive zone length L_c in a homogeneous medium of stiffness E^* and Poisson's ratio ν:

$$L_c = \frac{\pi}{8}\frac{E^*}{1-\nu^2}\frac{G_c}{\sigma_{ave}^2}. \tag{45}$$

In (45), G_c and σ_{ave} denote the fracture toughness and average cohesive strength of the material, respectively. A con-

Table 2
Cohesive properties used for the particle/blend interface

σ_c [MPa]	χ_c [μm]	G_c [J/m^2]	β
Interface 1			
1.0	0.75	2.039	0.9
Interface 2			
0.5	0.75	1.019	0.9

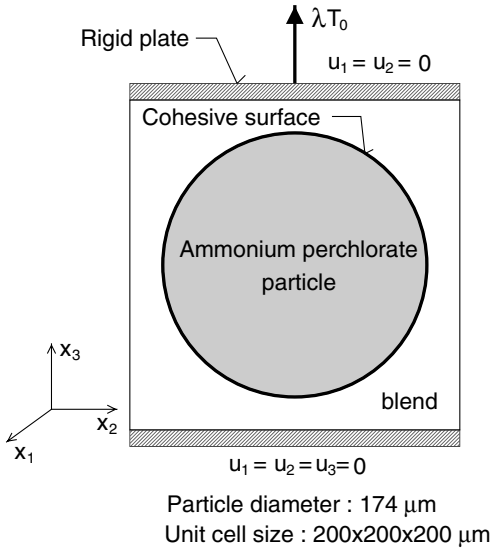

Fig. 3. Geometry and boundary conditions of the one-particle unit cell.

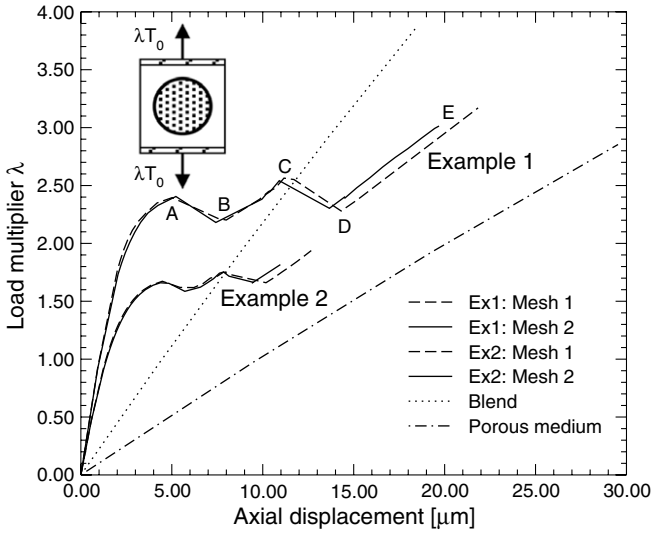

Fig. 4. Force–displacement curves for the one-particle unit cell: comparison of damage evolution for two interface strengths and two discretizations.

servative estimate of the cohesive zone size was obtained by substituting the properties of the more compliant blend in (45), together with the cohesive properties listed earlier. Two mesh discretizations were investigated to verify the spatial convergence of the solution. The first mesh uses a cohesive element size $h_e^c \approx L_c/3$, the second $h_e^c \approx L_c/6$. The characteristics of the finite element discretizations are listed in Table 3, where *nn* is the number of finite element nodes, *ne* represents the number of volumetric elements, *nce* denotes the number of cohesive element and *dof* is the number of degrees of freedom.

The load–displacement curves for both mesh discretizations, together with the response of a porous medium and a homogenized blend, are shown in Fig. 4. A good agreement is obtained between the solutions corresponding to the two meshes over the loading history, vouching for the spatial convergence of the numerical solution. The difference between the numerical solutions, at the larger strains (from point *C* to point *E*), is associated with the volumetric response of the surrounding binder, when the particle is substantially debonded and the matrix carries the most of the load and experiences substantial deformation.

Although the geometry and boundary conditions are symmetric, the decohesion process for mesh 2 initiates at the bottom of the particle due to the imperfections associated with the nonuniform discretization. Note that, for the coarser mesh 1, the decohesion process starts at the top of the particle. The resulting force–displacement behavior is however almost identical as shown in Fig. 4. A discussion on a possible bifurcation of the solution path is provided below.

Table 3
Details of the two finite element discretizations for the one-particle composite system

	nn	*ne*	*nce*	*dof*
Mesh 1	1629	6619	420	5754
Mesh 2	2913	12,997	684	10,511

The decohesion process computed with mesh 2 is depicted in a series of snapshots shown in Fig. 5, corresponding to the points labeled *A*–*E* on the force–displacement curve in Fig. 4. At point *A* of the loading process (Fig. 5*A*), the effective traction on the cohesive surface almost reaches its critical value. As loading continues, the bottom part of the particle debonds and the dewetting is accompanied by the rapid unloading of the top surface and decrease in the overall applied force (point *B* and Fig. 5*B*). The crack growth at the bottom of the particle and subsequent reloading of the top cohesive surface up to the critical value are shown in Fig. 5*C* (point *C*). The bottom of the particle is then unloaded and a second debonding initiates at the top of the particle, leading to the second drop of the applied force (Fig. 5*D* and point *D*). At this point, the particle is debonded on both sides and the cracks propagate along the matrix–particle interface (Fig. 5*E* and point *E*).

As expected, compressive forces are present along the particle equator at the end of the loading process preventing the complete decohesion of the particle and resulting in a damaged material that is stiffer than a porous medium. This fact can be observed in Fig. 6, which shows the effective cohesive tractions along the particle surface and the compressive ring arresting those tips in the equatorial region. The stiffening of material due to the circumferential constraint is also visible in Fig. 4, as the damaged material response lies between those of the undamaged blend (dotted line) and the fully porous system (dash-dotted curve).

Fig. 4 also shows the influence of the cohesive failure properties and, in particular, of the failure strength, on the load-displacement curve. The key features of the material response for the weak interface are similar to those described earlier for the stronger interface, with the same

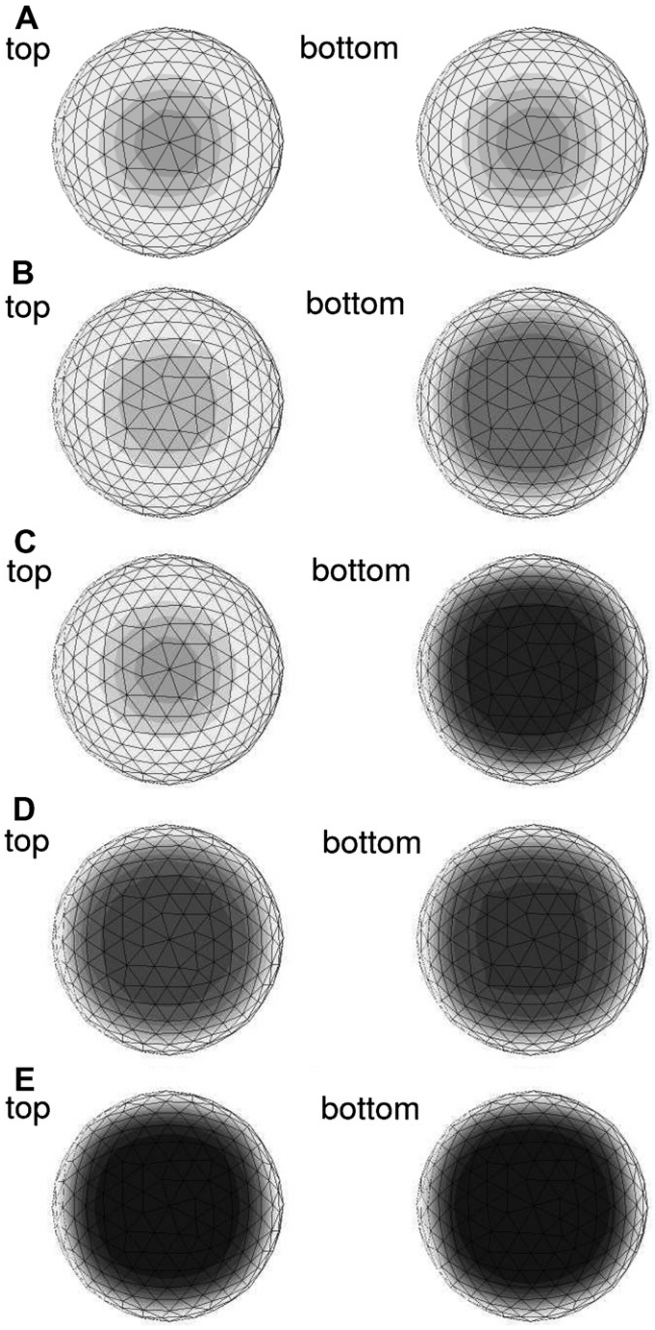

Fig. 5. Effective opening $\tilde{\chi}$ defined by (10) along the top and bottom cohesive surface obtained with mesh 2 at loading points labeled A–E in Fig. 4. All contour plots have the same scale, with the min (white) and max (black) values equal to 0 μm and 10 μm, respectively.

succession of peaks and valleys associated with the initiation of local debonding followed by unloading phases. However, due to the lower value of the critical traction, the maximum load reached before softening is lower for the weaker interface as shown in Fig 4. As expected, the material response of the fully damaged material (i.e., at the conclusion of the debonding process) is the same for both interface strengths.

Bifurcation is a common phenomenon in non-linear continuum mechanics and appears even in seemingly simple problems involving fairly standard constitutive models [42,21]. However, the direct detection of bifurcation points is not simple and requires a special numerical treatment [42]. Here we analyze the bifurcation of the solution obtained for two different loading histories. Note that, in this work, bifurcation points are not detected directly. The geometry, and boundary conditions are the same as above, with the fine discretization (Mesh 2) and the weak interface. Two loading histories characterized by different arc-length sizes are analyzed and lead to a bifurcation in the solution path, as illustrated in Fig. 7. As mentioned earlier, the solution labeled 1_A corresponds to the debonding of one of the poles of the spherical particle followed by the unloading of the opposite surface. As shown in Fig. 7, the second solution path exists for which both cohesive surfaces debond simultaneously, leading to the force–displacement curve labeled 2_A. The differences in the failure process can also be assessed from the opening displacement contour plots shown in Fig. 8.

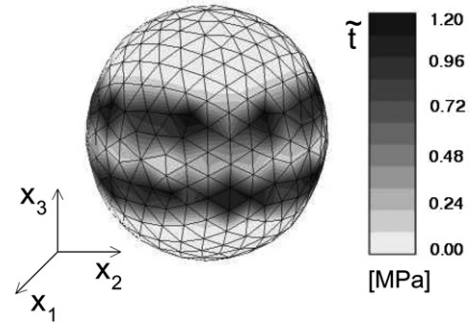

Fig. 6. Effective cohesive tractions at the end of the loading process (point E).

5.2. Four-particle composite system

We now turn our attention to a four-particle composite system to demonstrate the ability of the numerical scheme

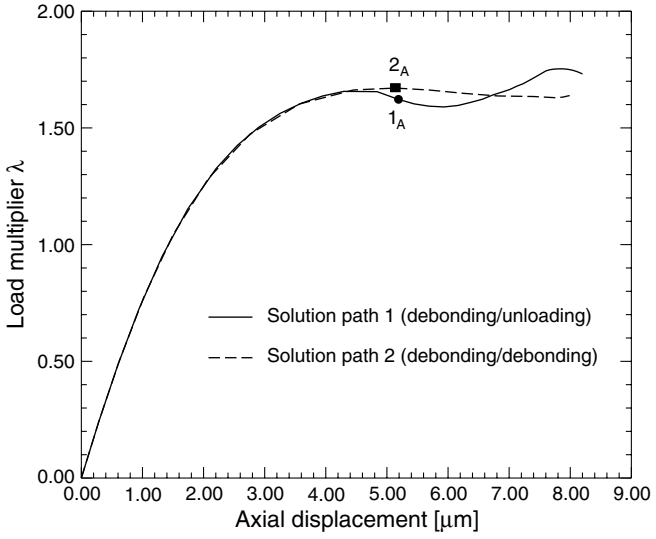

Fig. 7. Bifurcation: load–deflection curves for two solution paths.

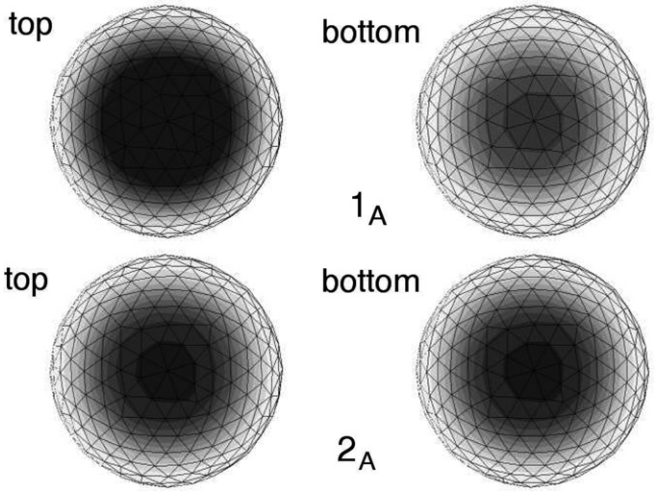

Fig. 8. Effective opening displacement for two solution paths shown in Fig. 7 at points 1_A and 2_A. Min (white) and max (black) values are 0 μm and 3 μm, respectively.

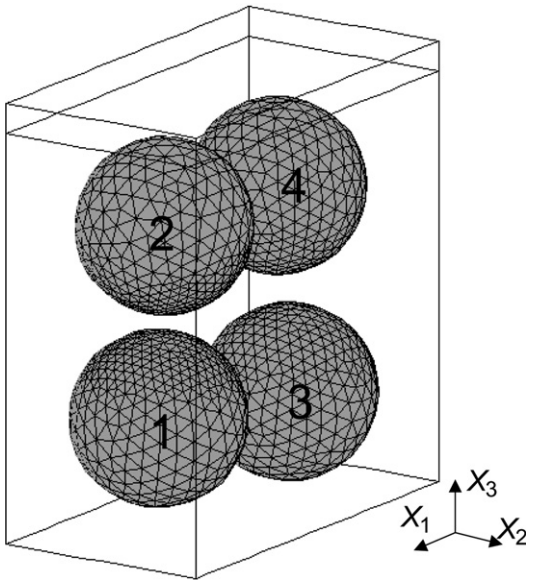

Fig. 9. Geometry and surface/cohesive mesh of four-particle unit cell.

to capture effects associated with nonuniform particle spacing and size. In the first example, we study the damage evolution in a composite medium composed of four randomly distributed spherical particles with the same diameter of 174 μm. The particles are dispersed in a unit cell of dimensions $420 \times 220 \times 410$ μm, yielding a moderate particle volume fraction of about 0.29. The unit cell is loaded by the same tensile force as in the previous examples. The other boundary conditions and material properties are also the same (Table 1). The adopted interface properties correspond to the second (weaker) interface listed in Table 2 and the mesh characteristics are listed in Table 4. The surface/cohesive mesh for the four-particle unit cell is shown in Fig. 9. The particles are not organized in a perfect lattice as the center coordinates are slightly perturbed as listed in Table 5.

Fig. 10 presents the force–displacement curves for the first four-particle unit cell problem. As expected, damage nucleates in the vicinity of the most closely packed particles (Particles 1 and 2), as illustrated in Fig. 11. The damage nucleation, denoted by point A on the force–displacement curve in Fig. 10, leads to a pronounced non-linear change of the force–displacement curve. However, due to the complex interactions between the particles, the damage evolution taking place at the microscale does not affect the average macroscopic response as drastically as for the single-particle unit cell. Although the particle diameters, the material and interfacial properties and volume fractions are almost identical, the resulting force–displacement curve for the four-particle unit cell remains monotonically increasing and does not display the softening and re-hardening regions shown in Fig. 4. The effective opening displacement distribution in the damaged medium (Point B in Fig. 10) is presented in Fig. 12, showing substantial debonding along the two more closely packed particles (1 and 2) and along particle 3. The accompanying unloading and the deformation of the matrix prevents the last particle (4)

Table 4
Finite element discretization for the unit cell composed of four particles of equal diameter

nn	*ne*	*nce*	*dof*
16,625	80,451	3702	64,109

Table 5
Particle center locations and diameter (given in μm) for the first four-particle unit cell problem

Particle #	X_1	X_2	X_3	∅
1	210	0	10	174
2	200	0	200	174
3	0	10	−10	174
4	−10	−10	190	174

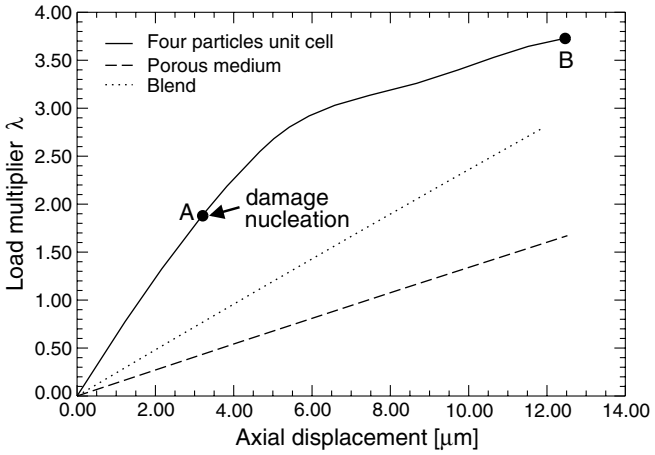

Fig. 10. Force–displacement curve for unit cell with four equal size particles.

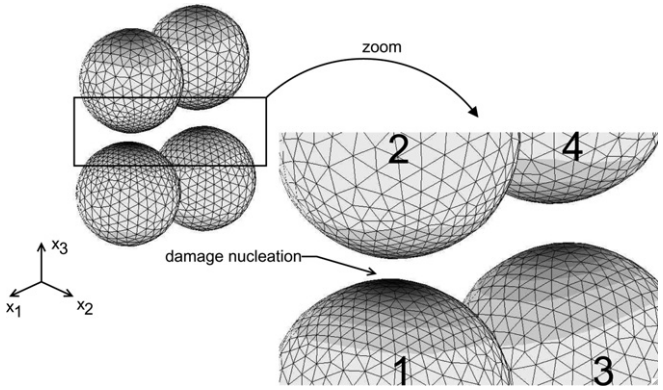

Fig. 11. Effective opening displacement distribution at damage nucleation (point A in Fig. 10) in the first four-particle unit cell problem. Min (white) and max (black) values are 0 μm and 0.75 μm, respectively.

to experience any damage along its lower surface at this stage of the loading process. To ensure uniform macroscopic deformation of the unit cell, damage is more pronounced along the top surface of particle 3. Debonding is also observed along particle surfaces located close to the top and bottom of the unit cell, probably due to the additional constraints associated with the rigid boundary conditions. The effective cohesive tractions acting along the particle surfaces are presented in Fig. 13, clearly showing the crack front location and the presence of compressive rings that lead to crack arrest. Higher axial loading of the unit cell would be required to achieve further damage in the model composite. However, the finite element mesh quickly becomes distorted due to the large deformations experienced by the matrix, requiring re-meshing or local mesh repair to guarantee the accuracy and convergence of the numerical scheme.

The second four-particle example is devoted to the influence of the particle diameter on the mechanical response and the damage nucleation. Particles of two different diameters (174 μm, 87 μm) are dispersed in the unit cell of dimensions $420 \times 220 \times 460$ μm yielding a small volume fraction of about 0.15. The unit cell is subjected to the same tensile force and boundary conditions as in the first example. The mechanical properties are listed in Table 1 and the

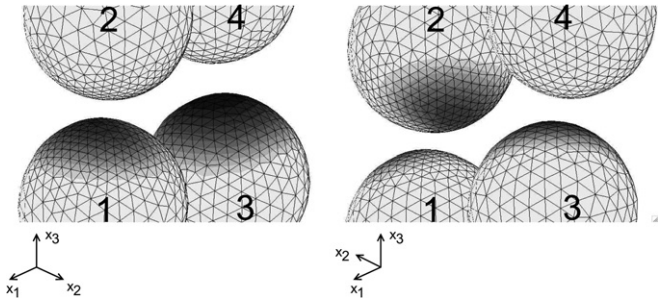

Fig. 12. Two views of the effective opening displacement distribution in damaged material (point B in Fig. 10) in the first four-particle unit cell problem. Min (white) and max (black) values are 0 μm and 8.6 μm, respectively.

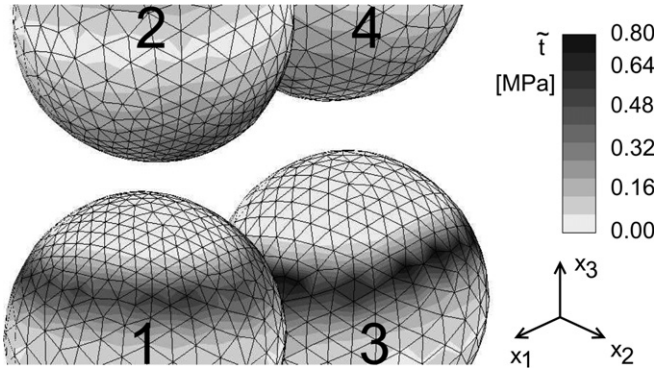

Fig. 13. Effective cohesive tractions for four-particle unit cell.

second (weaker) interface is selected again in this study (Table 2). The mesh characteristics are listed in Table 6. The particles are this time perfectly organized with center coordinates listed in Table 7. To minimize the influence of the top and bottom fixed boundaries, the reference box is enlarged in X_3 direction from 410 to 460 μm so that the distance from the large particles to the top and bottom boundaries of the unit cell is approximately equal to the center-particle distance.

Fig. 14 presents the force–displacement curves for the second four-particle unit cell problem. Due to the low particle concentration, the force–displacement curve is much closer to the response of the blend, and the difference between the blend and porous medium responses is decreased also. As typical for such systems, damage nucleates on the cohesive surface associated with the bigger particles. The effective cohesive opening at the early stage of damage is shown in Fig. 15. This corresponds to point A on the force–displacement curve in Fig. 14. Since the volume fraction of particles is low, the stiffness quickly deteriorates and the composite response is degraded almost to that of the blend (Fig. 14). Dilute reinforcement also makes the force–displacement curve monotonically increasing without softening and re-hardening regimes. The effective opening displacement distribution in the damaged medium

Table 6
Finite element discretization for the second four-particle unit cell problem with different particle diameters

	nn	*ne*	*nce*	*dof*
Mesh 1	16,952	85,587	1944	65,020

Table 7
Particle center locations and diameter (given in μm) for the second four-particle unit cell

Particle #	X_1	X_2	X_3	∅
1	200	0	0	174
2	200	0	200	87
3	0	0	0	87
4	0	0	200	174

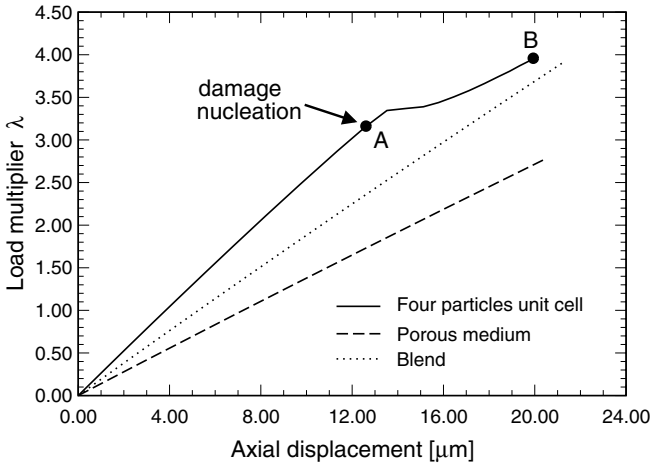

Fig. 14. Force–displacement curve for four-particle unit cell with different particle sizes.

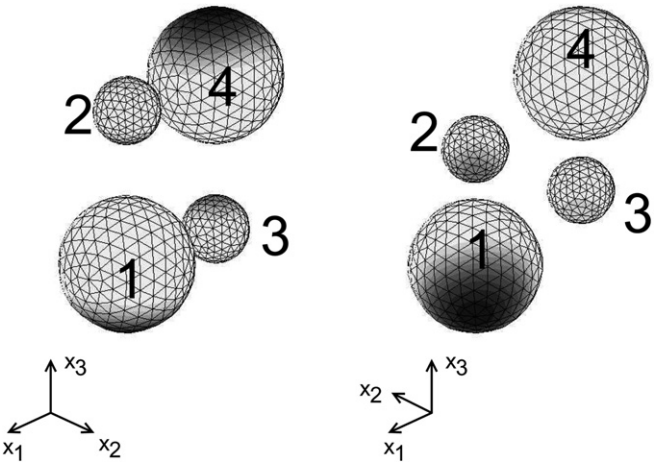

Fig. 16. Two views of the effective opening displacement distribution in damaged material (point *B* in Fig. 14) in the second four-particle unit cell problem. Min (white) and max (black) values are 0 μm and 7.3 μm, respectively.

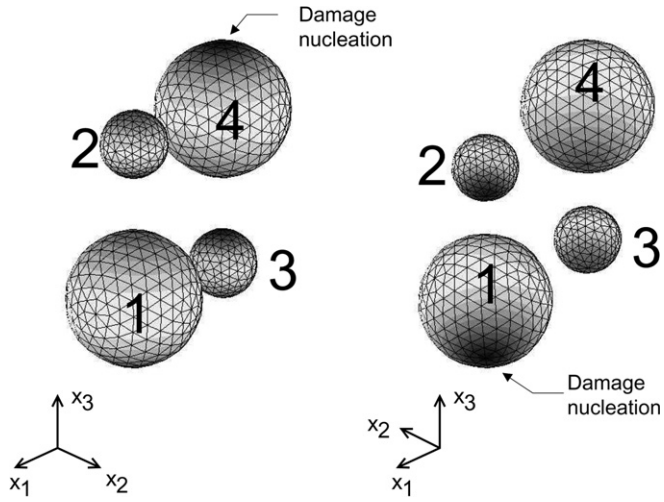

Fig. 15. Effective opening displacement distribution at damage nucleation (Point *A* in Fig. 14) in the second four-particle unit cell problem, showing damage nucleation along the larger particles. Min (white) and max (black) values are 0 μm and 0.90 μm, respectively.

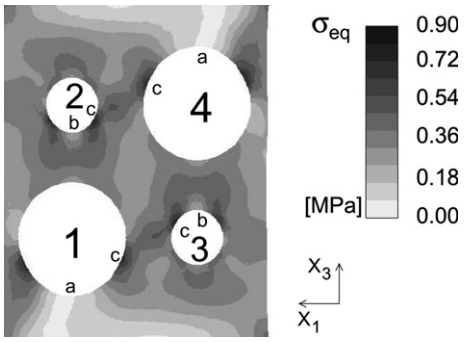

Fig. 17. Effective von Mises stress in the matrix (point *B* in Fig. 14) in the second four-particle unit cell problem. Labels "a" and "b" denote debonding of the large and small particles, while the stress concentration regions likely to lead to matrix failure are denoted by "c". The cut-off plane is $\boldsymbol{X} = \{0,0,0\}$.

(point *B* in Fig. 14) is presented in Fig. 16, displaying substantial debonding along the top (particle 4) and bottom (particle 1) cohesive surface. The smaller particles 2 and 3 are also debonded in the regions closer to the big particles 1 and 4, respectively. Further loading would be needed to complete the decohesion process. However, the large strains present in the matrix (about 12% at point *B*) lead to element distortion and make convergence and accuracy increasingly difficult. Once again, the re-meshing or local mesh repair would be required at this point. Fig. 17 displays the von Mises effective stress in the matrix. As apparent there, the bottom and top regions (points a in Fig. 17) of particles 1 and 4, respectively, are fully unloaded due to the progressive interfacial damage. The bottom and top regions (points b in Fig. 17) of particles 2 and 3 are also unloaded. Moreover, stress concentrations can be observed at the crack tips (points c in Fig. 17), which would most likely lead to tearing of the matrix and void coalescence. Since the geometry, boundary conditions and load are symmetric, the stress distribution shown in Fig. 17 holds the symmetry as well.

6. Conclusions

We have formulated and implemented a 3D computational model to simulate dewetting evolution in reinforced elastomers subject to finite strains. The particle–matrix interface is modeled by a cohesive law that accounts for irreversibility and mode mixity. The finite element framework is based on a stabilized updated Lagrangian formulation and adopts a decomposition of the pressure and displacement fields to eliminate the volumetric locking due to the nearly incompressible behavior of a matrix. The consistent linearization of the resulting system of

non-linear equations has been derived and leads to an efficient solution of the complex highly non-linear problem.

Through a set of examples involving one- and four-particle unit cells, we have shown the ability of the numerical scheme to capture the non-homogeneous stress and deformation fields present in the matrix and the damage nucleation and propagation along the particle–matrix interface. In particular, the scheme was shown to capture effects associated with the interface strength and nonuniform particle spacing and size. The existence of a bifurcation in the solution path was also briefly investigated.

The present work is a first step toward linking the macro-scale to the meso-scale through the computational homogenization, where a meso-structure is fully coupled with the deformation at a typical material point of a macro-continuum. The formulation and implementation of a truly multiscale model for the effect of microstructural damage on the macroscopic constitutive response of reinforced elastomers is the topic of our future research.

Acknowledgements

The authors gratefully acknowledge support from the Center for Simulation of Advanced Rockets (CSAR) at the University of Illinois, Urbana-Champaign. Research at CSAR is funded by the US Department of Energy as a part of its Advanced Simulation and Computing (ASC) program under contract number B341494.

References

[1] C.D. Bencher, R.H. Dauskardt, R.O. Ritchie, Microstructural damage and fracture processes in a composite solid rocket propellant, J. Spacecraft Rockets 32 (2) (1995) 328–334.
[2] J. Bergstrom, M.C. Boyce, Constitutive modeling of the large strain time-dependent behavior of elastomers, J. Mech. Phys. Solids 45 (5) (1998) 931–954.
[3] J. Bonet, R.D. Wood, Nonlinear Continuum Mechanics for Finite Element Analysis, Cambridge University Press, New York, NY, 1997.
[4] F. Brezzi, M. Fortin, Mixed and Hybrid Finite Element Methods, Springer, New York, NY, 1991.
[5] U. Brink, E. Stein, On some mixed finite element methods for incompressible and nearly incompressible finite elasticity, Comput. Mech. 19 (1996) 105–119.
[6] T.A. Davis, I.S. Duff, A combined unifrontal/multifrontal method for unsymmetric sparse matrices, ACM Trans. Math. Software 25 (1) (1999) 1–19.
[7] A. Dorfmann, R.W. Ogden, A constitutive model for the Mullins effect with permanent set in particle-reinforced rubber, Int. J. Solids Struct. 41 (2004) 1855–1878.
[8] A.K. Drozdov, A. Dorfmann, A micro-mechanical model for the response of filled elastomers at finite strains, Int. J. Plasticity 19 (2003) 1037–1067.
[9] G.J. Dvorak, M.V. Srinivas, New estimates of overall properties of heterogeneous solids, J. Mech. Phys. Solid 47 (1999) 899–920.
[10] J.D. Eshelby, The determination of the elastic field of an ellipsoidal inclusion and related problems, Proc. R. Soc. Lond. A-241 (1957) 376–396.
[11] J.R. Farris, The character of the stress–strain function for highly filled elastomers, Trans. Soc. Rheol. 12 (1968) 303–314.
[12] P.H. Geubelle, J.S. Baylor, Impact-induced delamination of composites: a 2D simulation, Composites Part B 29B (1998) 589–602.
[13] M. Kaliske, H. Rothert, Constitutive approach to rate-independent properties of filled elastomers, Int. J. Solids Struct. 35 (17) (1998) 2057–2071.
[14] K. Ha, R.A. Schapery, A three-dimensional viscoelastic constitutive model for particulate composites with growing damage and its experimental validation, Int. J. Solids Struct. 35 (26–27) (1998) 3497–3517.
[15] Z. Hashin, S. Shtrikman, On some variational principles in anisotropic and nonhomogeneous elasticity, J. Mech. Phys. Solids 10 (1962) 335–342.
[16] T.J.R. Hughes, L.P. Franka, M. Balestra, A new finite element formulation for computational fluid dynamics: V. Circumventing the Babuška–Brezzi condition: a stable Petrov–Galerkin formulation of the stokes problem accommodating equal-order interpolations, Comput. Methods Appl. Mech. Engrg. 59 (1986) 85–99.
[17] O. Klaas, A.M. Maniatty, S.M. Shephard, A stabilized mixed finite element method for finite elasticity. Formulation for linear displacement and pressure interpolation, Comput. Methods Appl. Mech. Engrg. 180 (1999) 65–79.
[18] Y.W. Kwon, C.T. Liu, Effect of particle distribution on initial cracks forming from notch tips in composites with hard particles embedded in a soft matrix, Composites B 32 (2001) 199–208.
[19] J. Lubliner, On thermodynamic foundations of non-linear solid mechanics, Int. J. Non-Linear Mech. 7 (1972) 237–254.
[20] J. Lubliner, On the structure of the rate equations of materials with internal variables, Acta Mech. 17 (1973) 109–119.
[21] J.E. Marsden, T.J.R. Hughes, Mathematical Foundations of Elasticity, Prentice-Hall, Englewood Cliffs, NJ, 1983.
[22] K. Matouš, Damage evolution in particulate composite materials, Int. J. Solids Struct. 40 (2003) 1489–1503.
[23] K. Matouš, A.M. Maniatty, Finite element formulation for modeling large deformations in elasto-viscoplastic polycrystals, Int. J. Numer. Methods Engrg. 60 (2004) 2313–2333.
[24] K. Matouš, P.H. Geubelle, Multiscale modeling of particle debonding in reinforced elastomers subjected to finite deformations, Int. J. Numer. Methods Engrg. 65 (2006) 190–223.
[25] C. Miehe, J. Keck, Superimposed finite elastic-viscoelastic-plastoelastic stress response with damage in filled rubbery polymers. Experiments, modelling and algorithmic implementation, J. Mech. Phys. Solids 48 (2000) 323–365.
[26] T.J. Oden, K.S. Vemaganti, Estimation of local modeling error and goal-oriented adaptive modeling of heterogeneous materials: Part I. Error estimates and adaptive algorithms, J. Comput. Phys. 164 (2000) 22–47.
[27] E. Oñate, J. Rojek, R.L. Taylor, O.C. Zienkiewicz, Finite calculus formulation for incompressible solids using linear triangles and tetrahedra, Int. J. Numer. Methods Engrg. 59 (2004) 1473–1500.
[28] M. Ortiz, A. Pandolfi, Finite-deformation irreversible cohesive element for three-dimensional crack-propagation analysis, Int. J. Numer. Methods Engrg. 44 (1999) 1267–1282.
[29] P.J. Rae, T.H. Goldrein, S.J.P. Palmer, J.E. Field, A.L. Lewis, Quasi-static studies of the deformation and failure of β-HMX based polymer bonded explosives, Proc. R. Soc. Lond. A-458 (2002) 743–762.
[30] G. Ravichandran, C.T. Liu, Modeling constitutive behavior of particulate composites undergoing damage, Int. J. Solids Struct. 32 (1995) 979–990.
[31] Y.A. Roy, R.H. Dodds, Simulation of ductile crack growth in thin aluminum panels using 3-D surface cohesive elements, Int. J. Fract. 110 (2001) 21–45.
[32] D. Rypl, Sequential and Parallel Generation of Unstructured 3D Meshes, Ph.D. dissertation, Czech Technical University in Prague, 1998.
[33] R.A. Schapery, Nonlinear viscoelastic and viscoplastic constitutive equations with growing damage, Int. J. Fract. 97 (1999) 33–66.
[34] J.C. Simo, K. Wriggers, K.H. Schweizerhof, R.L. Taylor, Finite deformation post-buckling analysis involving inelasticity and contact constraints, Int. J. Numer. Methods Engrg. 23 (1986) 779–800.

[35] J.C. Simo, R.L. Taylor, Consistent tangent operators for rate-independent elastoplasticity, Comput. Methods Appl. Mech. Engrg. 48 (1985) 101–118.
[36] J.C. Simo, On a fully three-dimensional finite-strain viscoelastic damage model: formulation and computational aspects, Comput. Methods Appl. Mech. Engrg. 60 (1987) 153–173.
[37] J.C. Simo, R.L. Taylor, K.S. Pister, Variational and projection methods for the volume constraint in finite deformation elasto-plasticity, Comput. Methods Appl. Mech. Engrg. 51 (1985) 177–208.
[38] H. Tan, Y. Huang, C. Liu, P.H. Geubelle, The Mori–Tanaka method for composite materials with nonlinear interface debonding, Int. J. Plasticity 21-10 (2005) 1890–1981.
[39] L.J. Walpole, On bounds for the overall elastic moduli of inhomogeneous system I, J. Mech. Phys. Solids 14 (1969) 151–162.
[40] L.J. Walpole, On bounds for the overall elastic moduli of inhomogeneous system II, J. Mech. Phys. Solids 14 (1969) 289–301.
[41] G.N. Wells, L.J. Sluys, A new method for modelling cohesive cracks using finite elements, Int. J. Numer. Methods Engrg. 50 (2001) 2667–2682.
[42] P. Wriggers, J.C. Simo, A general procedure for the direct computation of turning and bifurcation points, Int. J. Numer. Methods Engrg. 30 (1990) 155–176.
[43] X.P. Xu, A. Needleman, A numerical study of dynamic crack growth in brittle solids, Int. J. Solids Struct. 84 (1994) 769–788.
[44] A.X. Zhong, W.G. Knauss, Analysis of interfacial failure in particle-filled elastomers, J. Engrg. Mater. Technol. 119 (1997) 198–204.
[45] A.X. Zhong, W.G. Knauss, Effects of particle interaction and size variation on damage evolution in filled elastomers, Mech. Compos. Mater. Struct. 7 (2000) 35–53.